Active Learning-Based Estimation of Extreme Roll Motion in Beam Seas with Supervised Dimensionality Reduction and Gradient Approximation

Tomoki Takami[1] and Masaru Kitahara[2]

[1]Associate Professor, Graduate School of Maritime Sciences, Kobe University, 5-1-1 Fukaeminamimachi, Higashinada-ku, Kobe, Hyogo, 6580022, Japan. Email: takami@maritime.kobe-u.ac.jp

[2]Associate Professor, Faculty of Engineering, Hokkaido University, Kita 13, Nishi 8, Kita-ku, Sapporo, Hokkaido 0608628, Japan.

ABSTRACT

An efficient method is presented for estimating extreme nonlinear roll motion of a ship in beam seas under a given short-term sea state. In the aim of reducing the number of numerical simulations for roll motion simulation, this study employs an active-learning framework, in which the active subspace is used for supervised dimensionality reduction. The heteroscedastic Gaussian Process Regression (hGPR) is used for meta-modeling the limit state function for a given extreme value, addressing incomplete stochastic spaces due to the use of active subspace. Beyond just these implementations, a surrogate model of the roll motion, based on the Duffing oscillator with cubic damping and a parametrized roll excitation moment, is incorporated, by which one can further mitigate the computation time required to estimate gradient vectors of the limit state function. Numerical demonstrations are made using 1 degree-of-freedom (DOF) and 2 DOF roll motion models, introducing a three dimensional hull form for wave-induced roll excitation force. The latter model involves an implicit coupling with heave motion. Through a comprehensive comparison with crude

Monte Carlo Simulation (MCS) and First Order Reliability Method, it turned out that the present approach enables efficient and accurate estimation of the exceedance probability for an excessive roll angle.

INTRODUCTION

Excessive rolling of a ship can result in a serious marine accident (see Luthy (Luthy 2023)). Thus, many scholars have devised numerical models for wave-induced roll motion, ranging from the 1 degree-of-freedom (DOF) (Maki (Maki 2017) and Jensen (Jensen 2007)) to multi-DOF models (e.g. Delefortrie and Vantorre (Delefortrie and Vantorre 2021)), having accounted for the nonlinearity in roll motion. Further, the Computational Fluid Dynamics (CFD) has been implemented in the simulation by e.g. Jiang et al. (Jiang et al. 2020) and Silva and Maki (Silva and Maki 2021), reflecting an exact hull form together with the bilge keel effect. Having established well-validated numerical methods for nonlinear roll motion, however, probabilistic estimation of excessive roll angles remains a challenge yet. A central cause of the difficulty lies in the fact that the crude Monte Carlo Simulation (MCS) requires substantial runs of a numerical simulation, especially for small probability cases. It is known that the coefficient of variation (COV) of the MCS result is estimated as (e.g. see Echard et al. (Echard et al. 2011)):

$$COV = \sqrt{\frac{1 - P_f^{MCS}}{n_{MC} P_f^{MCS}}} \tag{1}$$

where P_f^{MCS} denotes the probability of exceedance of a certain threshold (hereafter referred to as "failure probability"), and n_{MC} the number of MCS computations. Evidently, to attain sufficiently small COV, for example $COV = 0.1$, to estimate $P_f^{MCS} = 1 \times 10^{-4}$, $n_{MC} = 1 \times 10^6$ MCS computations are required; meaning that the use of a high-fidelity numerical method like CFD is not feasible in an engineering context.

The First Order Reliability Method (FORM) and Second Order Reliability Method (SORM) are known as alternatives to MCS, through which efficient failure probability estimations can be achieved (Zhao and Ono (Zhao and Ono 1999)). However, the accuracy of FORM/SORM deteriorates if the response of interest exhibits strong nonlinearity, e.g. nonlinear roll motion (Jensen et al. (Jensen et al. 2017)). In pursuit of enhancing the accuracy of failure probability estimation while minimizing computational efforts, an active learning reliablity (ALR) method, , known as AK-MCS, was devised by Echard et al. (Echard et al. 2011), by combining MCS and Kriging, equivalently Gaussian Process Regression (GPR). Several variants of AK-MCS have been proposed thus far, with the aim of improving the stability and computational tractability of the ALR methods for, in particular, small failure probability problems, as exemplified by AK-SS (Huang et al. (Huang et al. 2016)), AK-IS (Echard et al. (Echard et al. 2013)), and AK-MCMC (Wei et al. (Wei et al. 2019)). More recently, the Bayesian ALR (BALR) methods have been devised, see e.g. Bect et al. (Bect et al. 2011) and Dang et al. (Dang et al. 2022a; Dang et al. 2022b). The BALR approaches frame the active learning process as a Bayesian inference problem and estimate the posterior distribution of the failure probability. The superiority of the BALR approaches over the conventional ALR approaches in terms of computational tractability has been demonstrated. Furthermore, novel sampling techniques have been incorporated into the BALR framework to address the complexity of posterior statics of the failure probability, as exemplified by Wei et al. (Wei et al. 2023) and Kitahara and Wei (Kitahara and Wei 2025). These (Bayesian) ALR methods, on the other hand, are beset by the well-known "curse-of-dimensionality"—that is, the computational burden associated with training the Kriging/GPR metamodel increases drastically as the dimensionality of the stochastic space increases. Extreme wave-induced response problems in a given short-term sea state entail a high-dimensional stochastic space needed to represent the incident wave spectrum, rendering the direct application of ALR methods impractical, if not impossible.

To overcome this difficulty, the authors' research group recently incorporated the Karhunen-Loève (KL) expansion of the stochastic wave (Sclavounos (Sclavounos 2012)), thereby reducing the number of stochastic variables, see Takami et al. (Takami et al. 2025). In conjunction with AK-MCMC (Wei et al. 2019), highly efficient estimations of extreme nonlinear vertical bending moment (VBM) in a ship were demonstrated. However, incorporating the KL expansion of wave is not a panacea for addressing other extreme wave-induced response problems; its benefit wanes if long-time numerical simulations are required. In fact, as attempted by Jensen (Jensen 2020), when nonlinear roll motion in beam seas is subjected to analysis, the failure probability estimation results (in ref. (Jensen 2020), FORM was used) were flawed, as the KL-based wave is only capable of representing short-time wave sequences in a reduced stochastic space.

Recently, the "active subspace" method proposed by Constantine (Constantine et al. 2014) has gained attention in the realm of reliability engineering, as a means of attaining *supervised dimensionality reduction* referring to a limited number of samples, see Jiang and Li (Jiang and Li 2017), Zhou and Peng (Zhou and Peng 2021), and Navaneeth and Chakraborty (Navaneeth and Chakraborty 2022). In the active subspace methodology, the low-dimensional feature space is detected with reference to samples of the limit state function and associated gradient vectors. By incorporating the active subspace into the active-learning process of GPR, in conjunction with the heteroscedasticity of GPR, Kim et al. (Kim et al. 2024) devised an adaptive active subspace-based heteroscedastic Gaussian process (AaS-hGP) methodology for high-dimensional extreme value estimation. The hGP can account for noise induced by input variables, whereby surrogate modeling with hGP works well even when the stochastic space is imperfect. The AaS-hGP sheds light on achieving efficient estimation of extreme nonlinear roll motion; however, gradient vector computations remain unavoidable insofar as the active subspace is employed, implying that scores of numerical computations are required apart from the limit state function calculations. If the finite difference method (FDM) is used for gradient calculation, as was employed in ref. (Kim et al. 2024), perturbative computations at the sampled points are required in this process, which in turn, a large number of numerical simulation runs in high-dimensional stochastic space are required. Thus, if a high-fidelity numerical model is utilized for roll motion computation, the original AaS-hGP method eventually imposes a significant computational burden.

To enhance the engineering feasibility of the AaS-hGP methodology for efficient nonlinear roll motion estimations, this paper newly proposes a gradient vector approximation (GVA) approach, making use of the Duffing oscillator together with a parametrized roll excitation moment as a surrogate model for the roll motion. Parameters in the surrogate model are identified with reference to the numerical simulation results at sampled points, followed by the GVA using the identified surrogate model. By incorporating the GVA into the AaS-hGP, high-fidelity numerical computations are only required at the sampled points during the training process of the hGP model. In this study, the Duffing oscillator with cubic damping, incorporating a parametrized roll excitation moment, is employed as the surrogate. Numerical demonstrations are conducted using 1 degree-of-freedom (DOF) and 2 DOF nonlinear roll motion models coupled with heave motion, where a 3D hull profile is utilized to derive the roll excitation moment.

AAS-HGP METHODOLOGY

This section introduces the AaS-hGP methodology presented by Kim et al. (Kim et al. 2024), which serves as an overall framework introduced in the present study.

Active subspace for supervised dimensionality reduction

Let the D-dimensional stochastic variables be $\boldsymbol{X} = [X_1,\ X_2,\ ..., X_D]$. Referring to the realization of $\boldsymbol{X}$ as $\boldsymbol{x}$, consider a continuous and differentiable function $y(\boldsymbol{x})$ and its gradient vector $\nabla_x y(\boldsymbol{x}) = \left[\frac{\partial y}{\partial x_1},\ \frac{\partial y}{\partial x_2},\ ..., \frac{\partial y}{\partial x_D}\right]^T$. In the present study, the function y serves as the limit state function for an extreme value of interest. That is,

$$y(\boldsymbol{x}) = 1 - \frac{\phi(t_f, \boldsymbol{x})}{\phi_f} \tag{2}$$

where $\phi(\boldsymbol{x})$ denotes the response value under the stochastic excitation of $\boldsymbol{x}$, t_f the point in time of interest, and ϕ_f the target extreme value. The probability corresponding to $y(\boldsymbol{X}) \leq 0$ is called the failure probability P_f. To retrieve a feature dimensional space by the active subspace (Constantine et al. 2014), the following $\boldsymbol{C}$ matrix is defined as:

$$\boldsymbol{C} = \int \nabla_x y \ \left(\nabla_x y\right)^T \rho \ \mathrm{d}\boldsymbol{x} \tag{3}$$

where ρ is the probability density function associated with $\boldsymbol{x}$. The following Monte Carlo integral (Navaneeth and Chakraborty 2022),

$$\hat{\boldsymbol{C}} = \frac{1}{N_{tr}} \sum_{i=1}^{N_{tr}} \left(\nabla_x y\right)_i \left(\nabla_x y\right)_i^T \tag{4}$$

is of practical use to assess $\boldsymbol{C}$ matrix based on N_{tr} training samples. $\boldsymbol{C}$ matrix is a positive semi-definite $D \times D$ matrix, admitting the following eigenvalue decomposition,

$$\boldsymbol{C} = \boldsymbol{W} \boldsymbol{\Lambda} \boldsymbol{W}^T \tag{5}$$

where

$$\boldsymbol{\Lambda} = diag\left\{\lambda_1, \lambda_2, \ ..., \lambda_D\right\} \tag{6}$$

where the eigenvalues meet $\lambda_1 \geq \lambda_2 \geq \ ... \geq \lambda_D \geq 0$. Matrices $\boldsymbol{W}$ and $\boldsymbol{\Lambda}$ can be split into two parts as:

$$\boldsymbol{\Lambda} = \begin{bmatrix} \boldsymbol{\Lambda}_r & \\ & \boldsymbol{\Lambda}_s \end{bmatrix}, \quad \boldsymbol{W} = \begin{bmatrix} \boldsymbol{W_r} & \boldsymbol{W_s} \end{bmatrix} \tag{7}$$

where $\boldsymbol{\Lambda_r}$ includes the largest d_r eigenvalues, i.e. $\boldsymbol{\Lambda_r} = diag\left\{\lambda_1, \lambda_2, \ ..., \lambda_{d_r}\right\}$. The projection matrix $\boldsymbol{W_r}$, with a size of $D \times d_r$, is called active subspace. Upon determining the order of the low-dimensional space d_r, the function $y(\boldsymbol{X})$ is approximated by using the low-dimensional feature vector $\boldsymbol{\Psi} \in \mathbb{R}^{d_r}$ defined as

$$\boldsymbol{\Psi} = \boldsymbol{W_r}^T \boldsymbol{X} \tag{8}$$

, which is characterized by the active subspace $\boldsymbol{W_r}$.

The dimensionality d_r is typically detected via a screening process of the eigenvalues to check whether a significant gap exists between λ_{d_r} and λ_{d_r+1} (Constantine et al. 2014). Nonetheless, in the present study, it is required that the function y can be adequately represented by the active subspace. With this in mind, the AaS-hGP procedure refers to the root mean squared error between the computed $y(\boldsymbol{x}_i)$ for N_{tr} training samples $\boldsymbol{x}_i$, $i = 1, 2, ..., N_{tr}$, and corresponding metamodel-based predictions (Kim et al. 2024):

$$\varepsilon_d = \sqrt{\frac{1}{N_{tr}} \sum_{i=1}^{N_{tr}} \{y(\boldsymbol{x}_i) - \mu_{\hat{y}}(\boldsymbol{\psi}_i)\}^2} \tag{9}$$

where $\boldsymbol{\psi}_i = \boldsymbol{W_r}^T \boldsymbol{x}_i$, cf. Eq. (8), and $\mu_{\hat{y}}$ denotes the mean of the surrogate model-based prediction. In the present study, $\mu_{\hat{y}}$ is driven by leveraging the hGP, see the subsequent sub-section 2. Referring to ε_d, d_r is detected via the following iterative process (Kim et al. 2024):

1. Prepare N_{tr} training samples and acquire $y(\boldsymbol{x}_i)$ and $\nabla_x y(\boldsymbol{x}_i)$.
2. Compute $\boldsymbol{C}$ and $\boldsymbol{W}$ according to Eqs. (4) and (5). Set $d_r = 1$
3. Train the hGP model based on $\boldsymbol{\psi}_i$ and $y(\boldsymbol{x}_i)$ in the low-dimensionality space $d_r = 1$
4. If $\varepsilon_d < \varepsilon_d^t$ or $d_r = D$, stop the iteration and accept the current d_r value. Otherwise, increment d_r by 1 and return to 3.

In the present study, $\varepsilon_d^t = 0.001$ is employed. In the early stages of AaS-hGP (in combination with FDM or GVA), the robustness of the hGP model based on d_r determined by Eq. (9) is marginal, due to the small number of training samples. Therefore, Eq. (9) is re-applied at every iteration of AaS-hGP to update d_r. The robustness of the hGP model and d_r is assessed by monitoring the convergence trend of the reliability index β, which is to be computed based on hGP predictions over all samples.

Metamodeling by Heteroscedastic Gaussian Process

Since the active subspace creation is made based on the limited number of training samples, the active subspace $\boldsymbol{W_r}$ detected during the training process is not necessarily *perfect*. Thus, given the low-dimensional projected variables $\boldsymbol{\psi} = \boldsymbol{W_r}^T\boldsymbol{x}$, the hGP accounts for the input-dependent noise to model the output y as:

$$y = f(\boldsymbol{\psi}) + \varepsilon(\boldsymbol{\psi}), \quad \varepsilon(\boldsymbol{\psi}) \sim \mathcal{N}\left(0, r(\boldsymbol{\psi})\right) \tag{10}$$

where

$$f(\boldsymbol{\psi}) \sim \mathcal{GP}(\mu_f(\boldsymbol{\psi}), k_f(\boldsymbol{\psi}, \boldsymbol{\psi'})), \quad r(\boldsymbol{\psi}) = \exp\{f_g(\boldsymbol{\psi})\} \tag{11}$$

where $f(\boldsymbol{\psi})$ denotes a latent function following a Gaussian process with mean $\mu_f(\boldsymbol{\psi})$ and covariance kernel $k_f(\boldsymbol{\psi}, \boldsymbol{\psi'})$, and $r(\boldsymbol{\psi})$ is the variance of the heteroscedastic noise. $f_g(\boldsymbol{\psi})$ in Eq. (11) also follows a Gaussian process, i.e. $f_g(\boldsymbol{\psi}) \sim \mathcal{GP}(\mu_0(\boldsymbol{\psi}), k_g(\boldsymbol{\psi}, \boldsymbol{\psi'}))$. Thus, the hGP is parametrized by using the hyperparameters $\{\boldsymbol{\theta}_f, \boldsymbol{\theta}_g, \mu_0\}$, where $\boldsymbol{\theta}_f$ and $\boldsymbol{\theta}_g$ are the hyperparameters for the kernel $k_f(\boldsymbol{\psi}, \boldsymbol{\psi'})$ and $k_g(\boldsymbol{\psi}, \boldsymbol{\psi'})$, respectively. To idendify the hyperparameters in the hGP, this study employs a variational approximation scheme proposed by Lázaro-Gredilla et al. (Lazaro-Gredilla et al. 2014). Details of the hyperparameter identification are given in I. Using identified hyperparameters, the hGP model offers the predictive mean $\mu_{\hat{y}}(\boldsymbol{\psi}_*)$ and standard deviation $\sigma_{\hat{y}}(\boldsymbol{\psi}_*)$ for a certain sample $\boldsymbol{\psi}_*$.

Active Learning of hGP Model

AaS-hGP employs an adaptive training process to efficiently construct the hGP model based on a sample population $\mathcal{W}_0^D = \{\boldsymbol{x}, \ldots, \boldsymbol{x}_N\}$ consisting of N pairs of the stochastic variables $\boldsymbol{X}$. To this end, given a whole N sample pool undergoing dimensionality reduction (i.e., $\mathcal{W}_0 = \left\{ \boldsymbol{W_r}^T \boldsymbol{x}_1, \ldots, \boldsymbol{W_r}^T \boldsymbol{x}_N \right\}$), and an existing N_{tr} training sample pool (i.e., $\mathcal{W}_{tr} = \left\{ \boldsymbol{W_r}^T \boldsymbol{x}_1, \ldots, \boldsymbol{W_r}^T \boldsymbol{x}_{N_{tr}} \right\}$), the next training sample $\boldsymbol{\psi}^*$ is detected by the following two steps:

1. From the whole sample pool $\mathcal{W}_0$, identify a subset $\mathcal{W}_c$ for which the so-called "U-function" obtained by the hGP predictions is less than 2. That is,

$$\mathcal{W}_c = \left\{ \boldsymbol{\psi} \in \mathcal{W}_0 : U(\boldsymbol{\psi}) = \frac{|\mu_{\hat{y}}(\boldsymbol{\psi})|}{\sigma_{\hat{y}}(\boldsymbol{\psi})} \leq 2 \right\} \tag{12}$$

2. Among the samples in $\mathcal{W}_c$, compute the minimum norm distance to the current training samples $\boldsymbol{\psi}'$ ($\in \mathcal{W}_{tr}$). Then, a sample in $\mathcal{W}_c$ that maximizes this minimum distance, denoted as $\boldsymbol{\psi}^*$, is selected as the next training sample. It means,

$$\boldsymbol{\psi}^* = \arg \max_{\psi \in \mathcal{W}_c} \left(\min_{\psi' \in \mathcal{W}_{tr}} \|\psi - \psi'\| \right) \tag{13}$$

Note that $U(\boldsymbol{\psi}) \leq 2$ is practically useful for various types of failure probability estimations, see e.g. refs. (Echard et al. 2011; Wei et al. 2019).

After detecting $\boldsymbol{\psi}^*$ in the low-dimensional space d_r, a convergence check of the training is made by referencing the failure probability P_f, which is derived by:

$$P_f \approx \frac{\sum_{i=1}^{N} \mathbb{I}\left(\mu_{\hat{y}}(\boldsymbol{\psi}) \leq 0\right)}{N} \tag{14}$$

where $\mathbb{I}\left(\mu_{\hat{y}}(\boldsymbol{\psi}) \leq 0\right) = 1$ if $\mu_{\hat{y}}(\boldsymbol{\psi}) \leq 0$, otherwise equal to 0. In ref. (Kim et al. 2024), the relative changes of P_f are monitored to determine the convergence of the active learning process. However, if P_f is relatively small, an instability in convergence performance was observed, as the simple counting by Eq. (14) evokes large variations in the relative P_f changes. As such, in the present study, the reliability index β, i.e.

$$\beta = -\Phi^{-1}(P_f) \tag{15}$$

where $\Phi(\cdot)$ denotes the cumulative distribution function of the standard normal distribution, is monitored. With reference to the reliability indices at the mth and $(m-1)$th learning steps, the following criteria

$$\varepsilon_1^{(m)} = \frac{\left|\beta^{(m)} - \beta^{(m-1)}\right|}{\beta^{(m)}} \tag{16}$$

$$\varepsilon_2^{(m)} = \left|\varepsilon_1^{(m)} - \varepsilon_1^{(m-1)}\right| \tag{17}$$

are monitored, and if both $\varepsilon_1^{(m)}$ and $\varepsilon_2^{(m)}$ are less than 0.0005, the learning process is terminated. Nonetheless, depending on the selection of the initial training samples, the learning process occasionally required a large number of iterations to satisfy the conditions $\varepsilon_1^{(m)} \leq 0.0005$ and $\varepsilon_2^{(m)} \leq 0.0005$. Hence, aprat from the convergence criteria given by Eqs. (16) and (17), the training process is terminated when the total number of training iterations reaches $m_{max} = 400$.

Fig. 1 shows an overall workflow of the present procedure based on the AaS-hGP methodology. It is anticipated that an excessively small initial sample size may lead to failure in estimating the active subspace and its dimensionality (i.e., d_r). In the present study, after preparing a whole $N = 10^6$ sample pool, the iterative scheme commences after referring to $N_0 = 100$ randomly selected initial samples, consulting ref. (Kim et al. 2024). As indicated in the workflow, the gradient vectors at the training samples are derived by either of the following methods: the direct FDM with perturbative computations, or the GVA to skip the perturbative computations.

GRADIENT VECTOR APPROXIMATION

Low-fidelity Model of Roll Motion

As mentioned earlier, the perturbative computations of a high-fidelity numerical model are computationally prohibitive, impeding the efficiency of the AaS-hGP method. It is known that the nonlinear roll motion in beam seas can be approximated by a computationally tractable second-order nonlinear differential equation, see e.g. Maki et al. (Maki et al. 2019) and Jensen (Jensen 2007). That being said, relevant parameters in the differential equation, i.e. damping and restoring terms, and the roll excitation moment by incident waves exhibit significant uncertainty. Thus, in the present framework, a parameter identification process is incorporated through which the roll motion computed by a high-fidelity numerical model can be appropriately reproduced by a parametrized low-fidelity nonlinear differential equation.

Despite its simplicity, the Duffing oscillator is known to be effective in modeling the nonlinear roll motion of a real ship, which is governed by nonlinear damping and restoring terms; see, e.g., Wawrzynski (Wawrzynski 2021) and Kougioumtzoglou et al. (Kougioumtzoglou et al. 2016). Hence, in the present study, the following model is employed as a low-fidelity model, which is fundamentally based on the Duffing oscillator together with cubic damping:

$$\ddot{\phi}_e + 2\xi_1\omega_0\dot{\phi}_e + \frac{\xi_3}{\omega_0}\dot{\phi}_e^3 + \frac{\omega_0^2}{GM}\left(k_1\phi_e + k_3\phi_e^3\right) = \frac{M_e(t)}{J_x} \tag{18}$$

where $\phi_e(t)$ denotes the instantaneous roll angle at time t, ξ_1 the linear damping, ξ_3 the cubic damping, k_1 the linear stiffness, k_3 the nonlinear stiffness, GM the transverse metacentric height, ω_0 the roll natural frequency, and M_e the roll excitation moment. J_x is characterized by the roll radius of gyration comprising the effect of added inertia $r_x = k_{xx}B$ as:

$$J_x = r_x^2 W = \left(k_{xx}B\right)^2 \rho_f LBTC_b \tag{19}$$

using the ship length L, breadth B, draught T, block coefficient C_b, and the fluid density $\rho_f = 1000\,(\mathrm{kg/m^3})$. The roll natural frequency holds the following relationship:

$$\omega_0 = \frac{\sqrt{gGM}}{k_{xx}B} \tag{20}$$

where $g = 9.81\,(\mathrm{m/s^2})$ denotes the acceleration of gravity. Summarizing up to this point, the roll motion $\phi_e(t)$ is characterized by the parameters $\{L, B, T, C_b, GM, k_{xx}, \xi_1, \xi_3, k_1, k_3\}$, apart from M_e.

M_e is in general characterized by using the transfer function (TRF) of the excitation moment w.r.t. the incident wave. Thus,

$$M_e(t) = \sum_{i=1}^{D/2} R(\omega_i)\sqrt{S(\omega_i)\mathrm{d}\omega_i}\left\{x_i \cos(\omega_i t + \Gamma(\omega_i)) - x_{i+D/2}\sin(\omega_i t + \Gamma(\omega_i))\right\} \tag{21}$$

where ω_i denotes the discretized wave frequency, $S(\omega_i)$ the incident wave spectrum, $\mathrm{d}\omega_i$ the non-equidistant frequency increment, and $\{R(\omega_i), \Gamma(\omega_i)\}$ the amplitude and phase of TRF. Note that for beam sea cases, $\Gamma(\omega_i) = -\frac{\pi}{2}$. As found from Eq. (21), the stochastic variables at a given sample $\boldsymbol{x} = \{x_1, x_2, ..., x_D\}$ are embedded to M_e and, in this case, $\boldsymbol{X}$ follows an uncorrelated standard normal distribution. It is evident that M_e is characterized by numerous parameters, as the TRF is discretized for each frequency ω_i. However, as the number of parameters increases, the parameter identification described later may become more challenging. To circumvent the growth in the number of parameters, this study employs the closed-form expression (CFE) for the TRF, proposed by Jensen et al. (Jensen et al. 2004). According to ref. (Jensen et al. 2004), $R(\omega_i)$ in beam seas is simply derived by using $\{L, B, T\}$ as:

$$R(\omega) = \sqrt{\frac{\rho_f}{\omega}}\, gL\sqrt{b_{44}}, \text{ where } b_{44} = \frac{1}{2}\rho_f B^3 T\sqrt{\frac{2g}{B}}\alpha_{bt}\exp\left\{\beta_{bt}\omega^{-1.3}\right\}\omega^{\gamma_{bt}} \tag{22}$$

where

$$\alpha_{bt} = 0.256\frac{B}{T} - 0.286 \tag{23a}$$

$$\beta_{bt} = -0.11\frac{B}{T} - 2.55 \tag{23b}$$

$$\gamma_{bt} = 0.033\frac{B}{T} - 1.419 \tag{23c}$$

By leveraging the CFE, one can efficiently model the excitation moment without increasing the number of parameters. Consequently, the present low-fidelity model offers the roll motion time series given the parameters $\boldsymbol{\Theta} = \{L, B, T, C_b, GM, k_{xx}, \xi_1, \xi_3, k_1, k_3\}$. The Runge-Kutta fourth-order method is used for solving Eq. (18), with the time increment of 0.5 s and the initial states $\phi_e(0) = 0$ rad, $\dot{\phi}_e(0) = 0$ rad/s.

Parameter Identification and Gradient Computation

During the active learning process, the roll motion time series corresponding to a training sample $\boldsymbol{x}^*$ is to be computed using a high-fidelity numerical model. Given the roll motion time series for the training sample $\phi\left(t_j, \boldsymbol{x}^*\right)$ at the instant time t_j, the following cost function is computed:

$$L\left(\boldsymbol{x}^*;\boldsymbol{\Theta}\right) = \sqrt{\frac{1}{N_t}\sum_{j=1}^{N_t}\left\{\phi\left(t_j, \boldsymbol{x}^*\right) - \phi_e\left(t_j, \boldsymbol{x}^*;\boldsymbol{\Theta}\right)\right\}^2} \tag{24}$$

where N_t denotes the number of discrete time points, and the parameter set $\boldsymbol{\Theta}$ is identified such that

$$\boldsymbol{\Theta}^* = \arg\min_{\boldsymbol{\Theta}}\left\{L\left(\boldsymbol{x}^*;\boldsymbol{\Theta}\right)\right\} \tag{25}$$

In the present study, the sequential quadratic programming (SQP) a maximum of 400 iterations is utilized to find $\boldsymbol{\Theta}^*$. The upper and lower bounds of the parameters

$$\{L, B, T, C_b, GM, k_{xx}, \xi_1, \xi_3, k_1, k_3\}$$

are set:

Lower bound: $\{0,\ 0,\ 0,\ 0,\ 0,\ 0.1,\ 0,\ 0,\ 0,\ -100\}$

Upper bound: {500, 50, 50, 1, 10, 1, 1, 1, 100, 100}

Among these, k_1 is constrained to positive values, thereby keeping ϕ_e being zero-mean. Upon derivation of $\mathbf{\Theta}^*$, the gradient vector at $\boldsymbol{x}^*$ is then estimated by using the low-fidelity model introducing $\mathbf{\Theta}^*$. In this study, a simple FDM is employed. It means, suppose that $\nabla_x y(\boldsymbol{x}^*) = [\Delta_1(\boldsymbol{x}^*), \Delta_2(\boldsymbol{x}^*), ..., \Delta_D(\boldsymbol{x}^*)]^T$,

$$\Delta_i(\boldsymbol{x}^*) = \frac{y_e(\boldsymbol{x}^* + \delta \boldsymbol{e}_i) - y(\boldsymbol{x}^*)}{\delta}, \text{ where } \ y_e(\boldsymbol{x}^* + \delta \boldsymbol{e}_i) = 1 - \frac{\phi_e(t_f, \boldsymbol{x}^* + \delta \boldsymbol{e}_i; \mathbf{\Theta}^*)}{\phi_f} \tag{26}$$

Although the FDM scheme necessitates the perturbative computations by Eq. (26), the computational burdens are small, thanks to the brevity of the model Eq. (18). Nonetheless, following the identification of parameters in the low-fidelity model, the adjoint method (see Givoli (Givoli 2021)) could enable a more efficient estimation of gradient vectors.

NUMERICAL INVESTIGATION

Numerical Model for Roll Motion

In the present study, the following two numerical models, a) 1 degree-of-freedom (DOF) roll model and b) 2 DOF roll model implicitly coupled with heave motion, which are based on Jensen (Jensen 2007), are used as *high-fidelity* models for numerical investigation. A bulk carrier used in ref. (Takami et al. 2024) is selected as a subject ship, see its principal particulars in Table 1. The models are:

a) 1 DOF model

$$\ddot{\phi} + 2\xi_{1,t}\omega_0\dot{\phi}_e + \xi_{2,t}\left|\dot{\phi}\right|\dot{\phi} + \frac{\xi_{3,t}}{\omega_0}\dot{\phi}_e^3 + \frac{\omega_0^2}{GM}GZ(\phi) = \frac{M_t(t)}{J_{x,t}} \tag{27}$$

b) 2 DOF model

$$\ddot{\phi} + 2\xi_{1,t}\omega_0\dot{\phi}_e + \xi_{2,t}\left|\dot{\phi}\right|\dot{\phi} + \frac{\xi_{3,t}}{\omega_0}\dot{\phi}_e^3 + \frac{\omega_0^2\left(1 - \frac{\ddot{h}}{g}\right)}{GM}GZ(\phi) = \frac{M_t(t)}{J_{x,t}} \tag{28}$$

where the damping terms $\{\xi_{1,t}, \xi_{2,t}, \xi_{3,t}\} = \{0.01, 0.073, 0.51\}$ are introduced based on the measurements in ref. (Takami et al. 2024). $J_{x,t}$ and ω_0 are derived with the introduction of principal particulars in Table 1 into Eqs. (19) and (20), respectively. h denotes the heave motion, and $\ddot{h}$ denotes the acceleration of heave. It is worth noting that Eq.(27) shares a similar structure to the low-fidelity model in Eq.(18), but the roll excitation moment M_t is derived in a more rigorous manner. The roll excitation moment $M_t(t)$ is computed in accordance with Eq. (21), but the TRF $R(\omega)$ is computed by a 3D panel theory-based code SPREME-web, see Matsui et al. (Matsui et al. 2024), with the 3D hull profile used as input. The transfer function of the roll excitation moment $R(\omega)$ computed by the 3D panel theory is shown in Fig. 2 by a red solid line. In the figure, $R(\omega)$ computed by the CFE with the introduction of $\{L, B, T\}$ in Table 1 is shown by a black solid line, for reference. One can find a significant difference between the 3D panel theory and CFE, which highlights the fact that the simple reference of $\{L, B, T\}$ cannot reproduce the roll excitation moment in a 3D hull, as the CFE in ref. (Jensen et al. 2004) assumes a simplified box-shaped hull.

The righting lever, GZ, is set by

$$GZ(\phi) = (GM - 1)\sin(\phi) + \phi + 15\phi^3 - 15\phi^5 \tag{29}$$

where the coefficients of ϕ, ϕ^3, and ϕ^5 are selected arbitrarily, but in such a way that the resulting GZ curve remains realistic. The resulting GZ curve is shown in Fig. 3, in comparison with a linear approximation by $GM \cdot \phi$. It is evident that the nonlinearity in the restoring force is prominent for large roll angles, specifically, larger than 0.3 rad. As for the incident wave spectrum, the Pierson-Moskowitz type wave spectrum with the significant wave height $H_s = 9$ m and the zero-upcrossing period $T_z = 10.5$ s is employed.

The acceleration of heave motion is computed by:

$$\ddot{h}(t) = \sum_{i=1}^{D/2} -\omega_i^2 R_h(\omega_i)\sqrt{S(\omega_i)\mathrm{d}\omega_i}\left\{x_i \cos(\omega_i t + \Gamma_h(\omega_i)) - x_{i+D/2}\sin(\omega_i t + \Gamma_h(\omega_i))\right\} \tag{30}$$

where $\{R_h(\omega_i), \Gamma_H(\omega_i)\}$ denotes the TRF of heave motion. In the present study, the CFE (Jensen et al. 2004) for heave motion is utilized to derive $\{R_h(\omega_i), \Gamma_H(\omega_i)\}$. The Runge-Kutta fourth-order method is used for solving Eqs. (27) and (28), with the time increment of 0.5 s and the initial states $\phi(0) = 0$ rad, $\dot{\phi}(0) = 0$ rad/s. The reference time t_f in Eq. (2) is set 600 s, so that the memory effects in the response are covered (Jensen 2007). Note that the KL expansion of the wave is no longer beneficial in such long-time numerical simulations, see (Takami et al. 2025). The target extreme value $\phi_f = 0.4$ rad is used.

The present 1 DOF and 2 DOF models are also based on nonlinear ordinary differential equations, like the low-fidelity model. However, the key difference is that the 1 DOF and 2 DOF models incorporate a) a realistic GZ curve (together with GM value) for restoring term characterization and b) wave-induced roll motion excitations, which are calculated using a full 3D ship hull model. It has been known that incorporating these factors together with together with the damping terms $\{\xi_{1,t}, \xi_{2,t}, \xi_{3,t}\} = \{0.01, 0.073, 0.51\}$ enables accurate reproduction of the actual roll motion of the vessel, see ref. (Takami et al. 2024), and in this context, the present 1 DOF and 2 DOF models can function as high-fidelity models.

Gradient Approximation Results

The accuracy of the present GVA scheme is first validated. For a single sample of stochastic variables $\boldsymbol{x}$, the parameter identification is carried out according to the procedure in Section 3. To find the parameters by SQP, the initial guess $\{L, B, T, C_b, GM, k_{xx}, \xi_1, \xi_3, k_1, k_3\} = \{278, 45, 17.7, 0.844, 5.47, 0.4, 0.1, 0.1, 0.1, 0\}$ is used, of which the principal parameters are referenced from Table 1 and the others are selected arbitrarily. Fig. 4 compares the roll motion time series computed via the 1 DOF model with the introduction of selected $\boldsymbol{x}$, the low-fidelity model computation (i.e. Eq. (18)) by the initial guess, and the low-fidelity model computation with identified parameters. Evidently, from the figure, the low-fidelity model together with identified parameters accurately reconstructs the 1 DOF model-based time series, despite the initial guess being poor in precision.

Four samples of $\boldsymbol{x}$ are taken to validate GVA results. For comparison, the FDM computations that directly incorporate the 1 DOF/2 DOF models—i.e., Eq. (26) with the substitution of the 1 DOF/2 DOF model results—are referenced as the authentic results (hereafter denoted as "direct FDM"). Figs. 5 and 6 compare the gradient vectors $\nabla_x y$ with respect to the dimension in $\boldsymbol{x}$. From Fig. 5, which refers to the 1 DOF model, the GVA results are highly correlated with the direct FDM results, despite subtle discrepancies. The same holds for the 2 DOF model cases, see Fig. 6, though the discrepancy is somewhat more pronounced compared to Fig. 5, which may be attributable to the heave motion contribution.

The gradient vector consequently influences the reduced dimensionality d_r and is subsequently reflected in the projection matrix $\boldsymbol{W_r}$, thereby affecting hGP model predictions. Therefore, the projection matrices $\boldsymbol{W_r}$ obtained from the direct FDM and the GVA, using the same initial training set (100 samples) for the 1 DOF model case are compared. The comparison is shown in Fig. 7, noting that $d_r = 29$ is detected by the direct FDM, whilst $d_r = 25$ by the GVA. Looking at Fig. 7, it is evident that the projection matrix obtained by the GVA captures the overall distribution of values comparable to that obtained by the direct FDM, without exhibiting any significant outliers, despite local discrepancies caused by deviations in the gradient vectors.

Putting the results into perspective, it is interpreted that the present GVA possesses the capacity to predict the gradient vectors to a certain extent, though not altogether accurately. Fortunately, the present approach employs the hGP, which allows the noise induced by the reduced feature space to be incorporated, suggesting that the small errors in $\boldsymbol{W_r}$ would not be a big deal.

The automatic differentiation, see e.g. Bolte and Pauwels (Bolte and Pauwels 2020), might have also provided approximations of the gradient vectors. However, it is anticipated that a sufficient number of samples of $y(\boldsymbol{x})$ would be required to ensure accurate gradient estimation. In fact, for the present cases with $D = 100$, thousands of samples may be necessary, which is somewhat too excessive.

Failure Probability Estimation Results

The failure probabilities associated with the limit state function Eq. (2) estimated by the AaS-hGP with and without the GVA scheme are then examined. For comparison, crude MCS computations are made with a sample size of $\boldsymbol{x}$ equal to 10^6, i.e. the 1 DOF/2 DOF models are to be computed 10^6 times in obtaining P_f. Apart from that, FORM computations based on the Modified Hasofer-Lind (M-HL) algorithm (Liu and Der Kiureghian, (Liu and Der Kiureghian 1991)) are also made for reference. The parameters used in the M-HL algorithm are configured in accordance with ref. (Takami et al. 2025). Attempts were made to introduce BALR approaches, specifically the Sequential and adaptive probabilistic integration (SAPI) (Kitahara and Wei 2025) and Parallel Adaptive Bayesian Quadrature (PABQ) (Dang et al. 2022b). However, both SAPI and PABQ failed to function properly due to memory limitations and were unable to produce a solution. This reminds us of the need for dimensionality reduction.

To examine the variation in the P_f estimates by AaS-hGP, 10 independent realizations of AaS-hGP are made by changing the sample pool $\mathcal{W}_0^D$. Fig. 8 indicates the mean and standard deviations of P_f for 1 DOF model derived from AaS-hGP with the introduction of direct FDM and GVA. From the figure, it is evident that, albeit a small difference in mean values between two approaches, the GVA-based AaS-hGP yields notably stable estimates on P_f, the standard deviation of which is reasonably small.

Comparisons of estimated failure probabilities and reliability indices by using each method are summarized in Tables 2 and 3. In the tables, N_{LSF} indicates the number of computations of limit state functions, that is, Eq. (2), by using the 1 DOF/2 DOF model, while N_{grad} indicates the number of required computations of 1 DOF/2 DOF model to obtain the gradient vectors during the AaS-hGP procedure. In this sense, $N_{grad} = N_{LSF}D$, if the direct FDM is integrated. Note that P_f (and corresponding β) and N_{LSF} from AaS-hGP indicated in Table 2 represent the mean values over 10 independent realizations. While the M-HL algorithm also incorporates the gradient vector computation stages, only the total numbers of required model evaluations are listed in the tables. The conversion between P_f and β is made according to Eq. (15). In Table 3, three distinct AaS-hGP results (with direct FDM or GVA) are indicated, which are denoted as "1st", "2nd", and "3rd", each obtained using a different initial training sample pool.

From the results, one can observe significant deviations in P_f obtained by FORM, compared to the crude MCS. This suggests that strong nonlinearity manifests in the respective limit state hypersurfaces, such that the linearization around the design point fails to approximate the failure probability. In contrast, P_f estimated by the AaS-hGP are much closer to those by the crude MCS. Note again that the AaS-hGP results exhibit some variability due to the selection of initial pool, say, in the Table 3 case, the β values range from 3.083 to 3.206; nevertheless, the accuracy remains remarkable. AaS-hGP has a key advantage in that it requires only a limited number of limit state function evaluations, as evidenced by N_{LSF} in the tables. However, if the direct FDM is utilized for computing gradient vectors, the total number of model evaluations, i.e. $N_{LSF} + N_{grad}$ is substantial. This issue will undoubtedly become more significant as the dimensionality D grows, or as the numerical model becomes more high-fidelity. Of note is the remarkable accuracy of the AaS-hGP with the introduction of GVA, in which the high-fidelity model evaluations are not required for gradient vector computations. Albeit the fact that the GVA necessitates the parameter identification schemes, the low-fidelity model Eq. (18) is computationally tractable, thereby the benefits of the GVA manifest when a high-fidelity model is referenced. As discussed in sub-section 4, the GVA exhibits relatively large deviations in the estimated gradient vectors, see Fig. 6, but Table 3 endorses that such differences do not have adverse effects on the P_f estimation results. It appears to be tempting to utilize the GVA in FORM as well; however, since the FORM analysis refers to the gradient vectors to compute the 'merit function' (Liu and Der Kiureghian 1991), small errors in the gradient vectors would be more problematic.

Fig. 9 shows the histories of the reliability index β by Eq. (15) during the iterative processes in the AaS-hGP. In the 1 DOF case, the "1st" realization results from AaS-hGP using the direct FDM and GVA are shown in the left-hand side figure, while in the 2 DOF model case, the "3rd" result from AaS-hGP (direct FDM) and the "1st" result from AaS-hGP (GVA) are shown in the right-hand side figure. Note that iteration number 0 corresponds to the starting point of the iteration referring to $N_0 = 100$ initial samples, thus the horizontal axis corresponds to m in Fig. 1. By and large, the AaS-hGP solutions start to converge after 150 iterations. β histories from three distinct runs of AaS-hGP for 2 DOF model case are shown in Fig. 10. On the surface, it appears that the convergence behavior differs between individual runs. In fact, for the "2nd" case of AaS-hGP (GVA), the convergence criteria given by Eqs. (16) and (17) are not satisfied until $m = m_{max}$, resulting in $N_{LSF} = N_0 + m_{max} = 500$. Having said that, all training processes demonstrate a clear trend toward convergence by 400 iterations.

In this study, convergence was assessed merely by referencing the relative variation of β, but discovering more appropriate and consistent convergence criteria warrants further investigation in future studies. Nevertheless, for practical use, one can monitor the β (or P_f) history during the process and terminate the iteration at one's own discretion, as the relative changes of β become subtle around 400 iterations.

CONCLUSION

In the present study, aiming at efficient estimation of extreme nonlinear roll motion, i.e. the failure probability associated with an excessive roll angle, an active learning-based methodology making use of the Heteroscedastic Gaussian Process (hGP) Regression was introduced. To deal with the high-dimensionality of stochastic ocean waves, a supervised dimensionality reduction technique, the so-called active subspace, was integrated. The basic procedure is called AaS-hGP methodology presented by Kim et al. (Kim et al. 2024). The original AaS-hGP procedure, in which the gradient vectors are evaluated by the direct Finite Difference Method (FDM), however, necessitates substantial computational burdens, as perturbative computations are required. To address this issue, in this study, the gradient vector approximation (GVA) scheme was proposed to enhance the computational efficiency. In the present GVA scheme, a Duffing oscillator-based low-fidelity roll motion model characterized by a limited number of parameters was utilized. By utilizing the low-fidelity model together with nonlinear optimization through the sequential quadratic programming (SQP), the parameters that best reproduce the high-fidelity numerical computation results are identified, and the gradient vector computations are undertaken by using the computationally tractable low-fidelity model. Thus, the benefit of GVA becomes more pronounced when the model of interest is more computationally demanding.

Numerical investigation was made using two high-fidelity models for roll motion, one is the 1 degree-of-freedom (DOF) model incorporating the roll excitation moment based on the 3D hull profile, while the other is the 2 DOF model in which an implicit coupling with heave motion is further integrated. By using the present GVA procedure, the gradient vectors can be reproduced to a reasonably accurate extent by the low-fidelity model together with identified parameters, albeit with slight deviations in the 2 DOF model cases. As regards the failure probability estimation, the AaS-hGP procedure demonstrated outstanding accuracy in the estimated failure probabilities, outperforming the First Order Reliability Method (FORM). The same was true even when the GVA scheme was introduced into the AaS-hGP. As such, the perturbative FDM computations using a high-fidelity model can be skipped, whereby enhancing the computational efficiency. Since the hGP is a metamodel that accounts for input-dependent noise, slight differences in the gradient vectors of the direct FDM did not have a significant impact on the failure probability.

This study utilized simplified roll motion models for numerical demonstration, but it is expected that the present AaS-hGP procedure together with GVA works well for real phenomena, as the present 1 DOF model can sufficiently describe the roll motion of a 3D ship, see Takami et al. (Takami et al. 2024). Therefore, the present approach may be applicable to the extreme roll motion estimation of a model ship by directly referencing measurements in a model basin; this will be addressed in the future. Further topics to be explored in the future include parametric rolling and the effect of nonlinearity in waves (see, e.g., West et al. (West et al. 1987)), as well as modifications to the AaS-hGP procedure to improve its applicability to rare events.

DATA AVAILABILITY STATEMENT

Some or all data, models, or code that support the findings of this study are available from the corresponding author upon reasonable request.

ACKNOWLEDGMENTS

This work was supported by JSPS KAKENHI (Grant Number 25K01432). The authors would like to acknowledge Dr. Jungho Kim, University of California, for sharing programming codes used to construct the hGP model.

APPENDIX I. HYPERPARAMETER IDENTIFICATION IN HETEROSCEDASTIC GAUSSIAN PROCESS MODEL

Lázaro-Gredilla et al. (Lazaro-Gredilla et al. 2014) proposed the following lower bound of the exact marginal likelihood using variational mean vector $\boldsymbol{m}$ and covariance matrix $\boldsymbol{V}$:

$$b_{MV}(\boldsymbol{m}, \boldsymbol{V}) = \ln \mathcal{N}(\mathcal{Y}_D; \mathbf{0}, \boldsymbol{K_f} + \boldsymbol{R}) - \frac{1}{4}\operatorname{tr}(\boldsymbol{V}) - \mathrm{KL}\left(\mathcal{N}(\boldsymbol{g}; \boldsymbol{m}, \boldsymbol{V}) \,\|\, \mathcal{N}(\boldsymbol{g}; \boldsymbol{\mu}_0 \mathbf{1}, \boldsymbol{K_g})\right) \quad (31)$$

where $\mathcal{Y}_D = \{y(\boldsymbol{x_1}), y(\boldsymbol{x_2}), ..., y(\boldsymbol{x_{N_{tr}}})\}$, $\operatorname{tr}(\cdot)$ denotes a trace operator, $\mathrm{KL}(\cdot|\cdot)$ the Kullback–Leibler divergence between two PDFs, $\boldsymbol{K_f}$ and $\boldsymbol{K_g}$ respectively are the covariance matrices of $f(\boldsymbol{\psi})$ and $f_g(\boldsymbol{\psi})$ in Eqs. (10) and (11), and $\boldsymbol{R}$ is a diagonal matrix with elements $R_{i,j} = \exp\{m_i - V_{i,j}/2\}$, $i = 1, 2, ..., N_{tr}$. The hyperparameters are to be identified so that this lower bound is maximized.

Upon identification of the hyperparameters, the predictive mean and variance of the limit state function corresponding to a given sample $\boldsymbol{\psi}_*$ can be given as:

$$\mu_{\hat{y}}(\boldsymbol{\psi}_*) = \boldsymbol{k}_{f_*}^T \left(\boldsymbol{K_f} + \boldsymbol{R}\right)^{-1} \mathcal{Y}_D, \quad (32)$$

$$\sigma_{\hat{y}}^2(\boldsymbol{\psi}_*) = \exp\left\{\chi_* + \eta_*^2/2\right\} + \gamma_*^2 \quad (33)$$

where χ_*, η_*^2, and γ_*^2 are:

$$\chi_* = \boldsymbol{k}_{g_*}^T \left(\boldsymbol{\Lambda_{MV}} - \frac{1}{2}\boldsymbol{I}\right) \mathbf{1} + \mu_0, \quad (34)$$

$$\eta_*^2 = k_{g**} - \boldsymbol{k}_{g_*}^T \left(\boldsymbol{K_g} + \boldsymbol{\Lambda}_{\boldsymbol{MV}}^{-1}\right)^{-1} \boldsymbol{k}_{g_*}, \quad (35)$$

$$\gamma_*^2 = k_{f**} - \boldsymbol{k}_{f_*}^T \left(\boldsymbol{K_f} + \boldsymbol{R}\right)^{-1} \boldsymbol{k}_{f_*} \quad (36)$$

where $\boldsymbol{k}_{f_*}$ amd $\boldsymbol{k}_{g_*}$ are vectors of covariance functions between the location $\boldsymbol{\psi}_*$ and N_{tr} training samples $\mathcal{W}_{tr} = \left\{\boldsymbol{W_r}^T \boldsymbol{x}_1, \ldots, \boldsymbol{W_r}^T \boldsymbol{x}_{N_{tr}}\right\}$ for latent functions $f(\boldsymbol{\psi})$ and $f_g(\boldsymbol{\psi})$, respectively. $\boldsymbol{\Lambda_{MV}}$ is a positive semi-definite diagonal matrix re-parameterizing $\boldsymbol{m}$ and $\boldsymbol{V}$ in a reduced order.

REFERENCES

Bect, J., Ginsbourger, D., Li, L., Picheny, V., and Vazquez, E. (2011). "Sequential design of computer experiments for the estimation of a probability of failure." *Statistics and Computing*, 22(3), 773–793.

Bolte, J. and Pauwels, E. (2020). "Conservative set valued fields, automatic differentiation, stochastic gradient methods and deep learning." *Mathematical Programming*, 188(1), 19–51.

Constantine, P. G., Dow, E., and Wang, Q. (2014). "Active subspace methods in theory and practice: Applications to kriging surfaces." *SIAM Journal on Scientific Computing*, 36(4), A1500–A1524.

Dang, C., Valdebenito, M. A., Faes, M. G., Wei, P., and Beer, M. (2022a). "Structural reliability analysis: A bayesian perspective." *Structural Safety*, 99, 102259.

Dang, C., Wei, P., Faes, M. G., Valdebenito, M. A., and Beer, M. (2022b). "Parallel adaptive bayesian quadrature for rare event estimation." *Reliability Engineering and System Safety*, 225, 108621.

Delefortrie, G. and Vantorre, M. (2021). "6dof manoeuvring model of kcs with full roll coupling." *Ocean Engineering*, 235, 109327.

Echard, B., Gayton, N., and Lemaire, M. (2011). "Ak-mcs: An active learning reliability method combining kriging and monte carlo simulation." *Structural Safety*, 33(2), 145–154.

Echard, B., Gayton, N., Lemaire, M., and Relun, N. (2013). "A combined importance sampling and kriging reliability method for small failure probabilities with time-demanding numerical models." *Reliability Engineering and System Safety*, 111, 232–240.

Givoli, D. (2021). "A tutorial on the adjoint method for inverse problems." *Computer Methods in Applied Mechanics and Engineering*, 380, 113810.

Huang, X., Chen, J., and Zhu, H. (2016). "Assessing small failure probabilities by ak–ss: An active learning method combining kriging and subset simulation." *Structural Safety*, 59, 86–95.

Jensen, J. J. (2007). “Efficient estimation of extreme non-linear roll motions using the first-order reliability method (form).” *Journal of Marine Science and Technology*, 12, 191–202.

Jensen, J. J. (2020). *Use of Prolate Spheroidal Wave Functions in the Time Domain First Order Reliability Method*. Springer Singapore, 760–769.

Jensen, J. J., Choi, J.-h., and Nielsen, U. D. (2017). “Statistical prediction of parametric roll using form.” *Ocean Engineering*, 144, 235–242.

Jensen, J. J., Mansour, A. E., and Olsen, A. S. (2004). “Estimation of ship motions using closed-form expressions.” *Ocean Engineering*, 31(1), 61–85.

Jiang, Y., Ding, Y., Sun, Y., Shao, Y., and Sun, L. (2020). “Influence of bilge-keel configuration on ship roll damping and roll response in waves.” *Ocean Engineering*, 216, 107539.

Jiang, Z. and Li, J. (2017). “High dimensional structural reliability with dimension reduction.” *Structural Safety*, 69, 35–46.

Kim, J., Wang, Z., and Song, J. (2024). “Adaptive active subspace-based metamodeling for high-dimensional reliability analysis.” *Structural Safety*, 106, 102404.

Kitahara, M. and Wei, P. (2025). “Sequential and adaptive probabilistic integration for structural reliability analysis.” *Structural Safety*, 114, 102577.

Kougioumtzoglou, I. A., Zhang, Y., and Beer, M. (2016). “Softening duffing oscillator reliability assessment subject to evolutionary stochastic excitation.” *ASCE-ASME Journal of Risk and Uncertainty in Engineering Systems, Part A: Civil Engineering*, 2(2).

Lazaro-Gredilla, M., Titsias, M. K., Verrelst, J., and Camps-Valls, G. (2014). “Retrieval of biophysical parameters with heteroscedastic gaussian processes.” *IEEE Geoscience and Remote Sensing Letters*, 11(4), 838–842.

Liu, P.-L. and Der Kiureghian, A. (1991). “Optimization algorithms for structural reliability.” *Structural Safety*, 9(3), 161–177.

Luthy, V. (2023). “Probability of occurrence of parametric roll on a predefined sea state.” Phd thesis, HESAM Université, HESAM Université.

Maki, A. (2017). “Estimation method of the capsizing probability in irregular beam seas using non-gaussian probability density function." *Journal of Marine Science and Technology*, 22, 351–360.

Maki, A., Sakai, M., and Umeda, N. (2019). "Estimating a non-gaussian probability density of the rolling motion in irregular beam seas." *Journal of Marine Science and Technology*, 24(4), 1071–1077.

Matsui, S., Takeda, K., and Sugimoto, K. (2024). "Difference in ship response in waves between strip and 3d methods based on integrated formulation." *Ocean Engineering*, 305, 117908.

Navaneeth, N. and Chakraborty, S. (2022). "Surrogate assisted active subspace and active subspace assisted surrogate—a new paradigm for high dimensional structural reliability analysis." *Computer Methods in Applied Mechanics and Engineering*, 389, 114374.

Sclavounos, P. D. (2012). "Karhunen–loeve representation of stochastic ocean waves." *Proceedings of the Royal Society A: Mathematical, Physical and Engineering Sciences*, 468(2145), 2574–2594.

Silva, K. M. and Maki, K. J. (2021). "Towards a computational fluid dynamics implementation of the critical wave groups method." *Ocean Engineering*, 235, 109451.

Takami, T., Kitahara, M., Jensen, J. J., and Matsui, S. (2025). "Extreme nonlinear ship response estimations by active learning reliability method and dimensionality reduction for ocean wave." *Marine Structures*, 99, 103723.

Takami, T., Nielsen, U. D., Jensen, J. J., Maki, A., Matsui, S., and Komoriyama, Y. (2024). "Onboard identification of stability parameters including nonlinear roll damping via phase-resolved wave estimation using measured ship responses." *Mechanical Systems and Signal Processing*, 210, 111166.

Wawrzynski, W. (2021). "Duffing-type oscillator under harmonic excitation with a variable value of excitation amplitude and time-dependent external disturbances." *Scientific Reports*, 11(1).

Wei, P., Tang, C., and Yang, Y. (2019). "Structural reliability and reliability sensitivity analysis of extremely rare failure events by combining sampling and surrogate model methods." *Proceedings of the Institution of Mechanical Engineers, Part O: Journal of Risk and Reliability*, 233(6), 943–957.

Wei, P., Zheng, Y., Fu, J., Xu, Y., and Gao, W. (2023). "An expected integrated error reduction function for accelerating bayesian active learning of failure probability." *Reliability Engineering and System Safety*, 231, 108971.

West, B. J., Brueckner, K. A., Janda, R. S., Milder, D. M., and Milton, R. L. (1987). "A new numerical method for surface hydrodynamics." *Journal of Geophysical Research: Oceans*, 92(C11), 11803–11824.

Zhao, Y.-G. and Ono, T. (1999). "A general procedure for first/second-order reliabilitymethod (form/sorm)." *Structural Safety*, 21(2), 95–112.

Zhou, T. and Peng, Y. (2021). "Active learning and active subspace enhancement for pdem-based high-dimensional reliability analysis." *Structural Safety*, 88, 102026.

List of Tables

TABLE 1. Principal particulars of a bulk carrier for numerical investigation

L(m)	B(m)	T(m)	C_b	GM(m)	k_{xx}
278	45	17.7	0.844	5.47	0.37

TABLE 2. Comparison of failure probabilities, reliability indices, and the number of required computations among each method (1 DOF model). The results shown for AaS-hGP are the mean values obtained from 10 realizations.

	crude MCS	FORM	AaS-hGP (direct FDM)	AaS-hGP (GVA)
P_f	1.10×10^{-3}	3.77×10^{-3}	1.17×10^{-3}	1.38×10^{-3}
β	3.061	2.672	3.043	2.993
N_{LSF}	10^6	32759	330	359
$N_{grad}(= N_{LSF}D)$	0		33000	0

TABLE 3. Comparison of failure probabilities, reliability indices, and the number of required computations among each method (2 DOF model).

	crude MCS	FORM	AaS-hGP (direct FDM)	AaS-hGP (GVA)
P_f	6.45×10^{-4}	2.29×10^{-3}	1.03×10^{-3} (1st) 9.75×10^{-4} (2nd) 6.73×10^{-4} (3rd)	5.18×10^{-4} (1st) 6.31×10^{-4} (2nd) 8.49×10^{-4} (3rd)
β	3.218	2.835	3.083 3.098 3.206	3.281 3.224 3.139
N_{LSF}	10^6	23656	352 219 275	461 500 (=$N_0 + m_{max}$) 329
$N_{grad}(= N_{LSF}D)$	0		35200 21900 27500	0

List of Figures

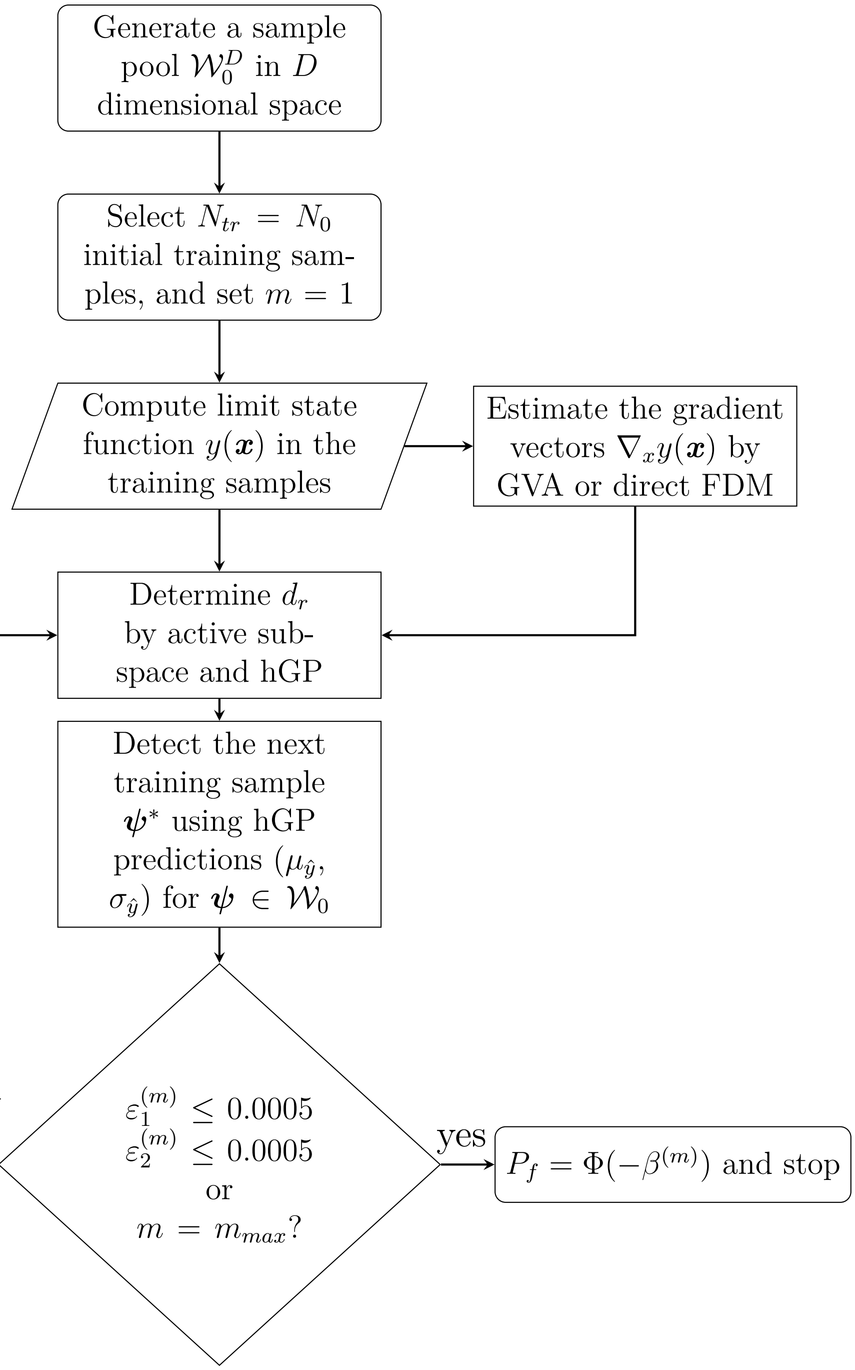

Fig. 1. Overall workflow of the active learning by active subspace and hGP

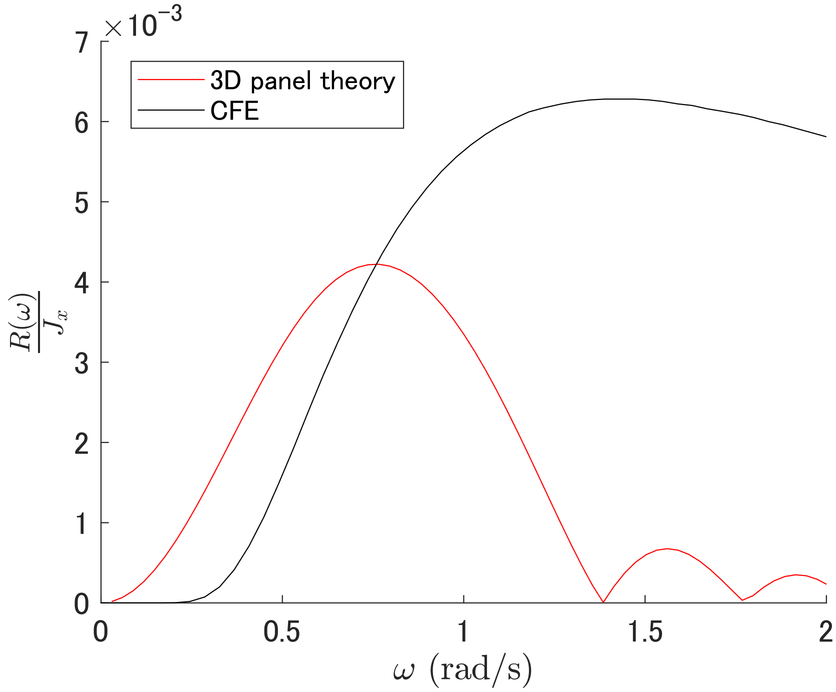

Fig. 2. Transfer functions (amplitude) of roll excitation moment derived from the 3D panel theory and closed-form expression

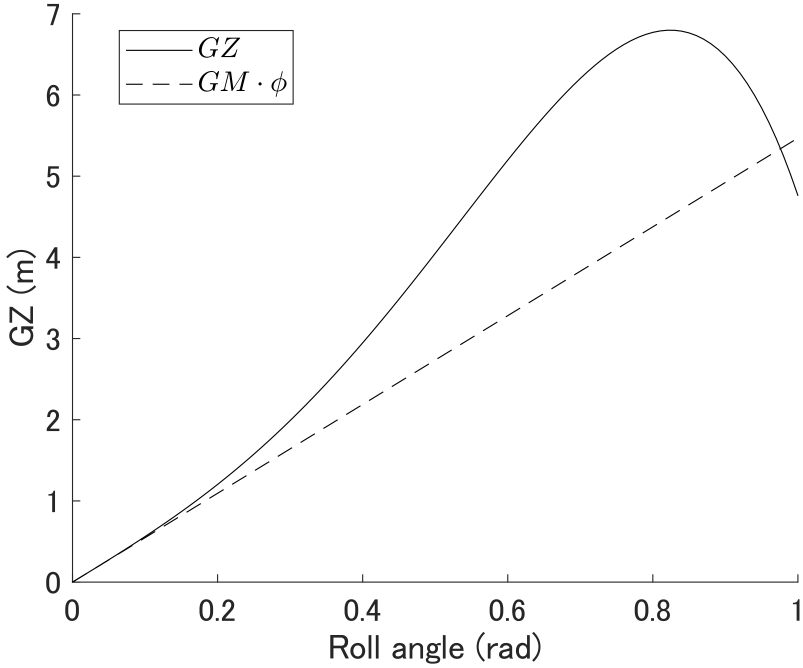

Fig. 3. Righting lever GZ of the bulk carrier

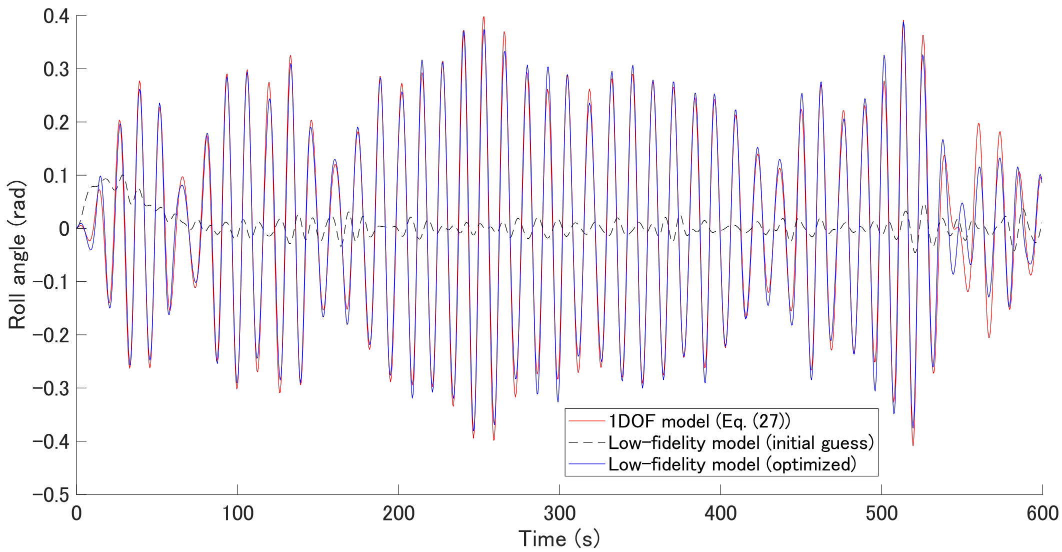

Fig. 4. Comparison of roll motion time series from 1DOF model (Eq. (27)) and low-fidelity model estimations

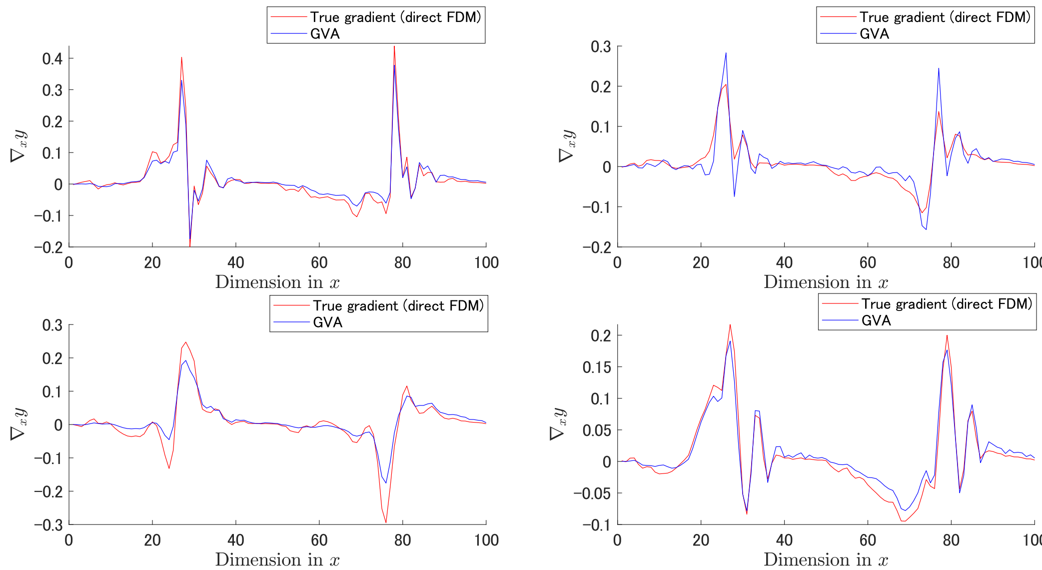

Fig. 5. Comparison of gradient vectors of the limit state function obtained by the direct Finite Difference Method and the present gradient vector approximation (GVA). 1 DOF model case.

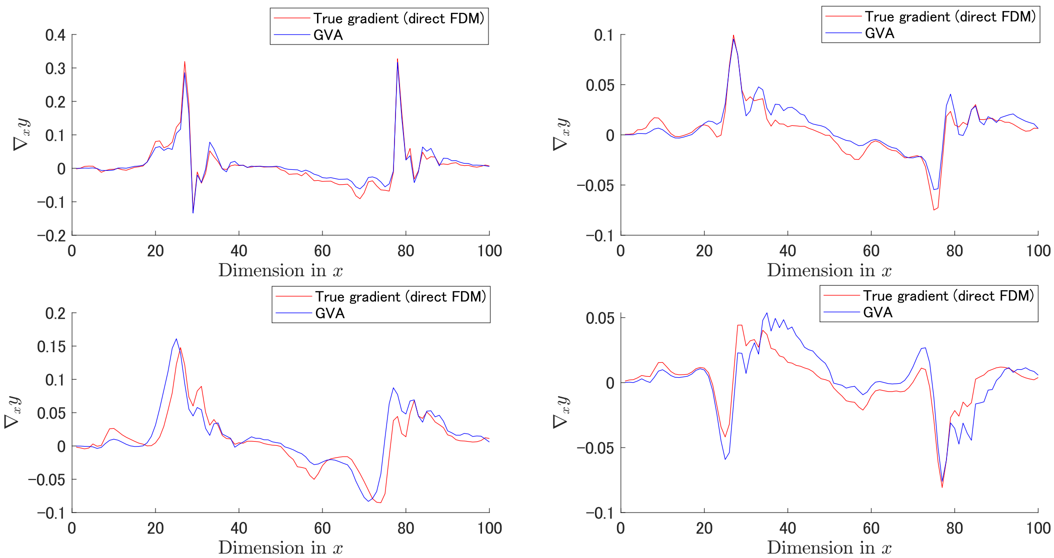

Fig. 6. Comparison of gradient vectors of the limit state function obtained by the direct Finite Difference Method and the present gradient vector approximation (GVA). 2 DOF model case.

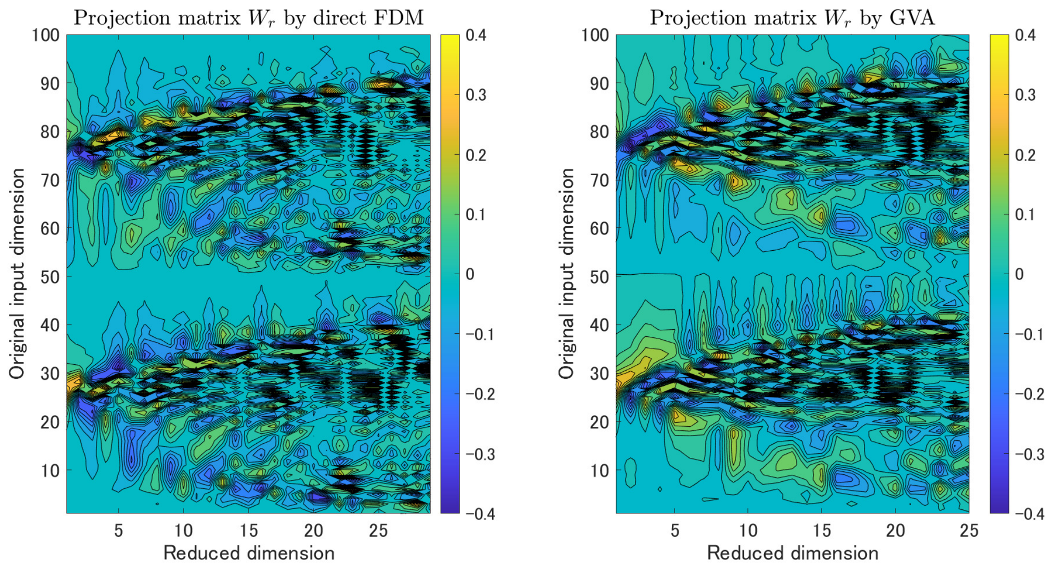

Fig. 7. Comparison of the projection matrix $\boldsymbol{W_r}$ obtained by the direct Finite Difference Method and the present gradient vector approximation (GVA). 1 DOF model case.

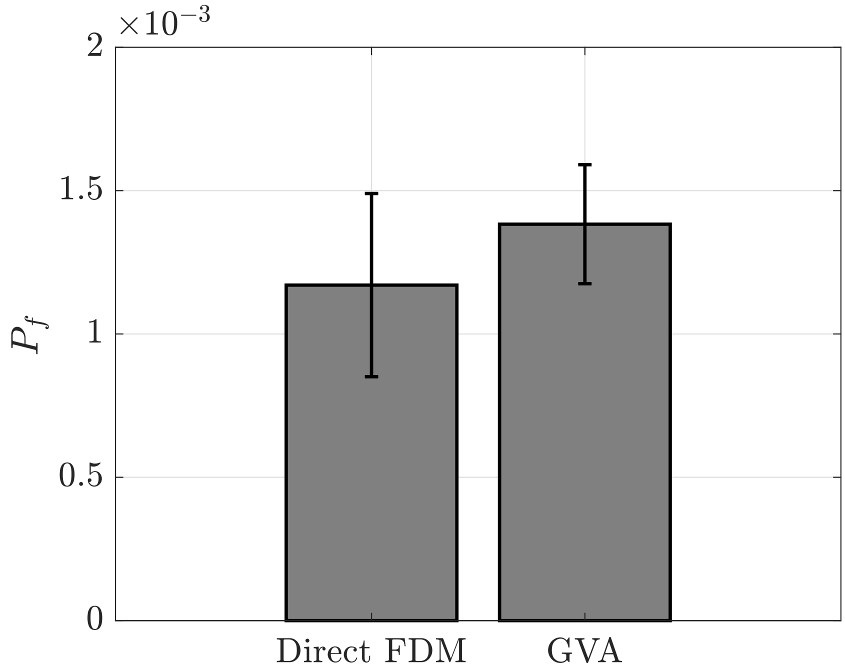

Fig. 8. Mean and standard deviation of P_f derived from 10 runs of AaS-hGP using the direct FDM and GVA. The bars indicate the mean values while the error bars indicate the ± 1 standard deviations. 1 DOF model case.

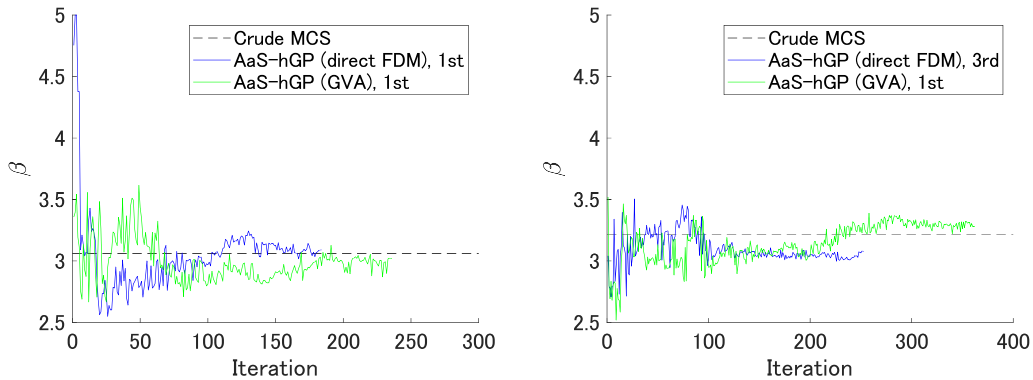

Fig. 9. Histories of reliability indices during the iteration in the AaS-hGP by 1 DOF model cases (left) and 2 DOF model cases (right)

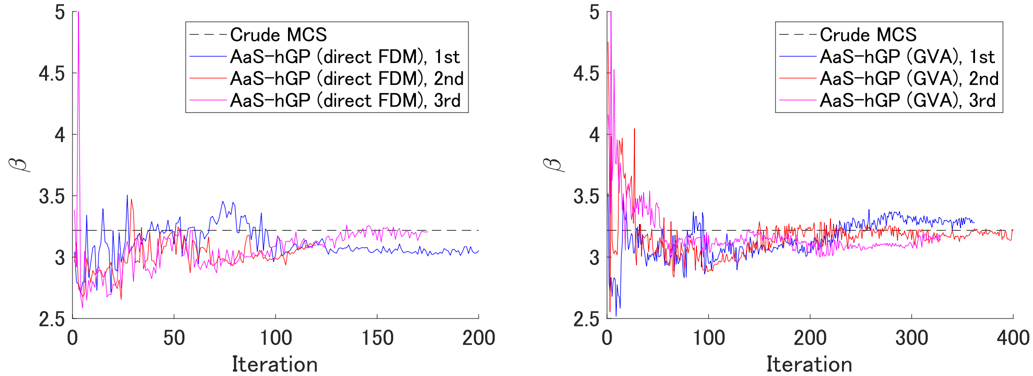

Fig. 10. Histories of reliability indices during the iteration in the AaS-hGP by 2 DOF model case from three distinct results, based on direct FDM (left) and GVA (right)